Structural fabrication of a ring-type motion sensor

2004 J. Micromech. Microeng. 14 710

(http://iopscience.iop.org/0960-1317/14/5/008)

INSTITUTE OF PHYSICS PUBLISHING JOURNAL OF MICROMECHANICS AND MICROENGINEERING

J. Micromech. Microeng. **14** (2004) 710–716 PII: S0960-1317(04)67384-0

Structural fabrication of a ring-type motion sensor

Jui-Hong Weng[1], Wei-Hua Chieng[1] and Jenn-Min Lai[2]

[1] Department of Mechanical Engineering, National Chiao Tung University, 1001 Ta Hsueh Road, Hsinchu, Taiwan, Republic of China
[2] MEMS Department, OPTO TECH Corporation, No 1, Li-hsin Road 5, Hsinchu Science-Based Industrial Park, Hsin-chu, Taiwan, Republic of China

E-mail: whc@cc.nctu.edu.tw

Received 8 August 2003
Published 17 March 2004
Online at stacks.iop.org/JMM/14/710 (DOI: 10.1088/0960-1317/14/5/008)

Abstract
The structural fabrication of a ring-type motion sensor is described. This micromachined ring-type sensor can be used to detect both yaw rate and linear acceleration. The fabrication is based on deep silicon etching and wafer bonding. An aspect ratio dependent effect (ARDE) always occurs in the dry etching process for a micro electromechanical systems (MEMS) device. Additionally, three processes are developed and modified progressively for eliminating ARDE from the fabrication results. Results indicate that the proposed process provides more flexibility than other processes with respect to the structural fabrication of a MEMS device. The sensitivity of the sensor characteristic to the manufacturing errors is considered as well.

1. Introduction

Sensors for detecting motion have been extensively investigated and developed over the last few decades. The gyroscope and accelerometer are two important types of inertial technologies for detecting motion. Sensor technology has migrated from discrete, expensive and inflexible units to smart, self-calibrating, silicon-based devices, which are integrated, low-cost, small, and offer other advantageous characteristics [1–3]. The rapid development of semiconductor technology has enabled micro electromechanical systems (MEMS), including micromachined gyroscopes and accelerometers, to keep up with the requirements of modern sensors.

The vibrating string gyro, the tuning fork gyro and the vibrating shell gyro sense the rate of rotation [5]. All of them can be implemented using MEMS technology, and some have been further realized [4–24]. The accelerometer has been used in many engineering applications for decades and many successful designs have been mass-produced [25–31]. The vibrating ring-type gyroscope and the capacitive accelerometer can be integrated into a single motion sensor that detects both acceleration and rotation. The vibration of a circular ring can be theoretically decoupled into several modes. The first mode corresponds to linear motion, and the second mode involves rotation. Two independent vibration modes exist concurrently. Therefore, the vibrating ring has great potential to integrate both the accelerometer and the gyroscope [32].

Silicon micro-machining processes for fabricating vibratory gyroscopes fall into one of four categories: (1) silicon bulk micromachining and wafer bonding, (2) poly-silicon surface micromachining, (3) metal electroforming and LIGA and (4) combined bulk and surface micromachining or so-called mixed processes [33]. The process proposed in this work falls into the first category. The device can be fabricated in numerous ways. Silicon bulk micromachining and wafer bonding technologies are used in this work and they follow from the structural design and the capacitive detection scheme. The main frame of the structure sits on the plane of the silicon wafer. The structural stiffness along the z-axis should be as large as possible to minimize the coupling of vibrations along different axes. Hence, deep silicon etching is used to form a bulk structure. Besides, detecting and driving schemata based on the electrostatic force would be more effective for relatively large capacitances. A larger capacitance corresponds to a deeper structure. Deep silicon etching technique for forming high-aspect-ratio structures must be used to ensure good detection performance. Anodic bonding is utilized to bond silicon to the glass. It is a mature technique and is used herein to create the suspended structure.

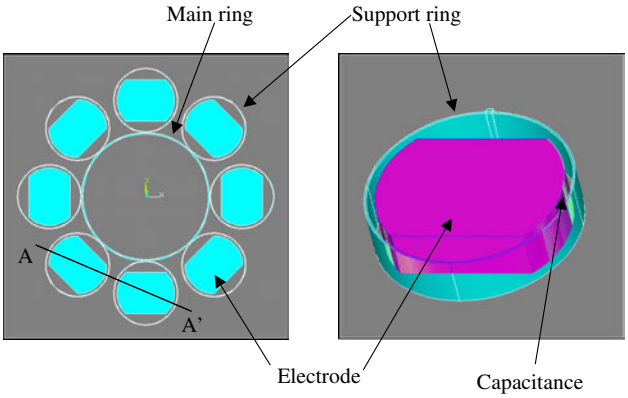

Figure 1. Top and detailed views of structure, including electrodes.

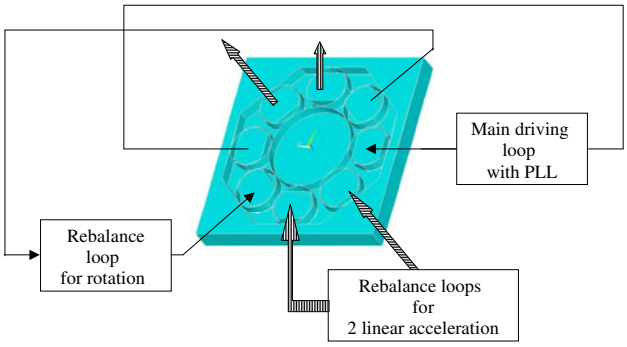

Figure 2. Schematic overview of control loops and structure.

2. Structure of the sensor

The sensor design consists of a structure and a control loop. Figure 1 depicts the top view of the structure of the sensor. The main ring in the center is the main body designed to vibrate in a flexural mode. Figure 2 reveals how the main ring is connected to eight support rings that surround it. The similarity between the shape of the main ring and that of the support rings simplifies the analysis. The main ring and the support rings are designed to vibrate in-plane, as depicted in figure 3. Electrodes are arranged at the centers of the support rings, as shown in figure 1, forming capacitors and driving the structure. The potential difference between the support ring and electrode generates an electrostatic force that attracts them toward each other, and drives the structure to vibrate. The electrodes are shaped to maximize effective displacement when the structure vibrates in the desired second mode of vibration.

Figure 2 schematically shows the control loops used to manipulate the sensor. The main driving loop causes the structure to vibrate as desired. The vibration is enhanced by phase-locked loops, and the structure vibrates at the resonant frequency to yield large amplitude [34]. A rebalancing loop is designed to rebalance the vibration induced by the Coriolis force. Two rebalancing loops are designed to balance the vibration induced by linear motion. Three rebalancing loops cooperate to balance the planar motion.

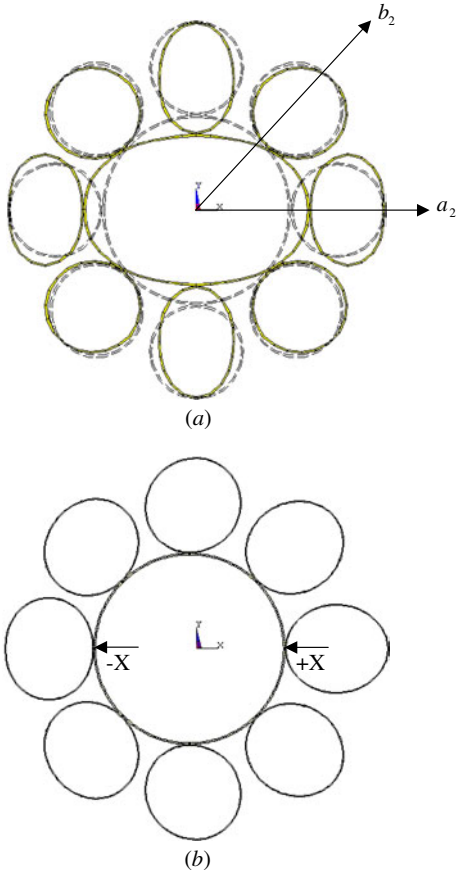

Figure 3. Scheme for detecting rotation and linear acceleration of (*a*) a gyroscope and (*b*) an accelerometer.

3. Fabrication

Three processes are developed for fabricating the structure of the motion sensor. They are modified to reduce the ARDE and are described as follows. The process described in the following sections is observed along $\overline{AA'}$ indicated in figure 1.

Figure 4 shows the first method of fabricating the sensor. The process begins with a $\{1, 0, 0\}$ n-type silicon wafer, which is patterned using photo-resist, as depicted in figure 4(*a*). The patterned wafer is etched with deep silicon etching by ICP etcher, as depicted in figure 4(*b*). The etched silicon wafer is bonded to a glass wafer by anodic bonding, as depicted in figure 4(*c*). The upper part of the composite wafer is removed by back-sided wet-etching and the structure is formed, as indicated in figure 4(*d*). The structure is then released by wet etching the glass wafer, as indicated in figure 4(*e*). Ideally, the etching rate is uniform at every position on the wafer. During deep etching, the RIE lag appears in the narrow trench. This effect is known as the aspect ratio dependent effect (ARDE). Figure 4(*b*) plots the RIE lag in the capacitor gap. The capacitor gap is 2 μm wide, as shown in figure 1. During the wet etching of the backside, some part, not on the capacitor gap, will be etched through first, as presented in figure 4(*d*). Intuitively, etching could be continued through the gap. However, this aforementioned structure has a high aspect ratio. Etching through the silicon wafer causes permanent damage to the wall of the structure. The structure will not be

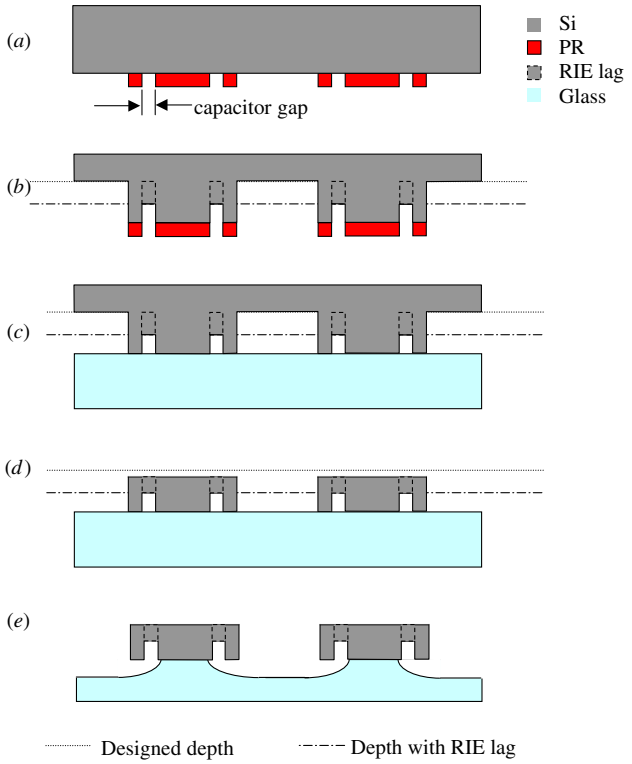

Figure 4. Fabrication by method I: (*a*) silicon patterning using photo resist, (*b*) deep silicon etching, (*c*) anodic bonding, (*d*) back-sided wet etching and (*e*) releasing of structure.

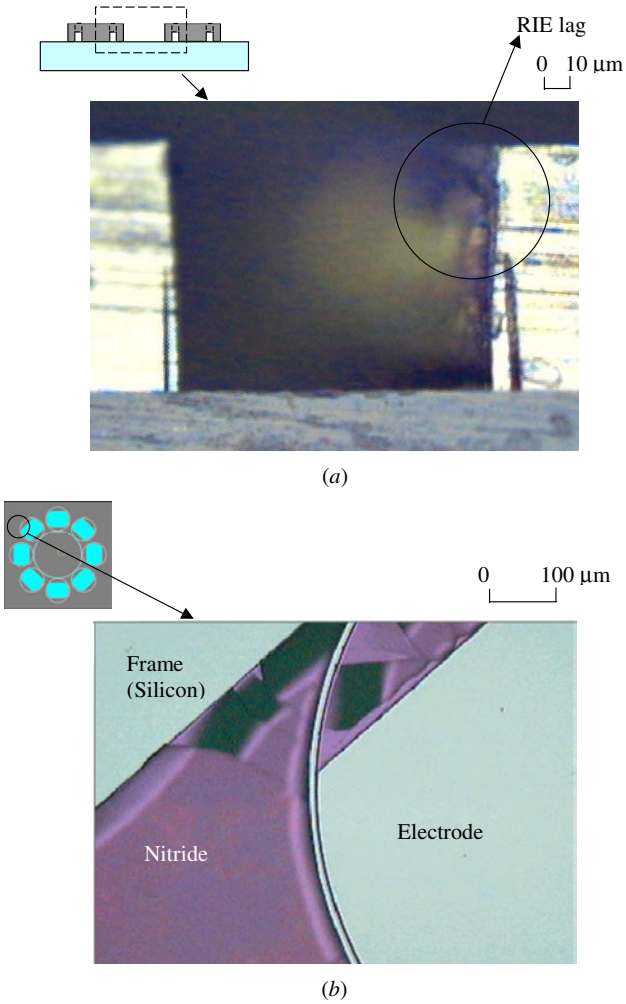

Figure 5. Photographs of the ring-type motion sensor fabricated by the process shown in figure 4. (*a*) Side view of the structure, with ARDE shown; (*b*) top view of a corner of the structure, 20 μm high.

released until the removal of the RIE lag part of the structure, as depicted in figure 4(*e*). Figure 5(*a*) presents the side view of the unreleased structure, which has formed a 100 μm-high wall. Reducing the etching depth reduces ARDE and the RIE lag. Figure 5(*b*) presents the structure with a 20 μm-high wall. However, the final structure is not sufficiently strong to prevent structural warping. The ARDE is negligible for the designed 20 μm-high structure.

An alternative means (method II) of modifying the process is to add a protective layer and dummy fields. Figure 6 schematically describes method II. The dummy field can be used to reduce the RIE lag in dry etching, as plotted in figure 6(*b*). The RIE lag is not entirely eliminated, because the dummy field should be sized so as not to affect the performance of the sensor. Hence, the gap between the structure and the dummy field is wider than that between the structure and the electrode. The protective layer is added after dry etching and before anodic bonding, as depicted in figure 6(*c*). This protective layer must be suitable to undergo the anodic bonding process. Hence, oxide and nitride are the candidate materials for this layer. This layer will protect the wall of the structure as long as the silicon is etched through in a back-sided wet etching process. The protective layer should resist the etchant until the RIE lag part is removed. The etchant used in wet etching must be isotropic. The height of the structure can be estimated from the following formula,

$$H = \frac{tS}{L_{\mathrm{RIE}}}(1 - L_{\mathrm{RIE}}), \qquad (1)$$

where H is the height of the structure, t is the thickness of the protective layer, S is the selectivity of the etchant, and L_{RIE} is the RIE lag ratio. The protective layer used in this case is nitride, and its thickness is 2000 Å. A thicker layer does not favor anodic bonding. The etchant used is HNA. The etching selectivity is 60. The dummy fields reduce the RIE lag ratio to 0.2. The height of the structure with the protective layer is estimated to be up to 40 μm, when the protective layer is included. When the protective layer is etched away and the silicon is exposed, as described above, etching can be performed 20 μm more deeply, without being affected by the ARDE. Hence, a 60 μm (40 μm + 20 μm) structure is accordingly fabricated, and is presented in figure 7.

The third method improves upon method II. The dummy field is sized to equalize the widths of all trenches (gaps) on the wafer, effectively eliminating ARDE and the RIE lag, as presented in figures 8(*a*) and (*b*). Unlike in method II, the dummy fields must be removed. A 2 μm step between the bonding region and non-bonding region is etched before the PR coating process is performed to remove the dummy field, as indicated in figure 8(*a*). The dummy fields cause negligible RIE lag in the deep silicon etching process. The protective layer is deposited on silicon, as depicted in figure 8(*c*), and a 2000 Å oxide is used herein. This layer

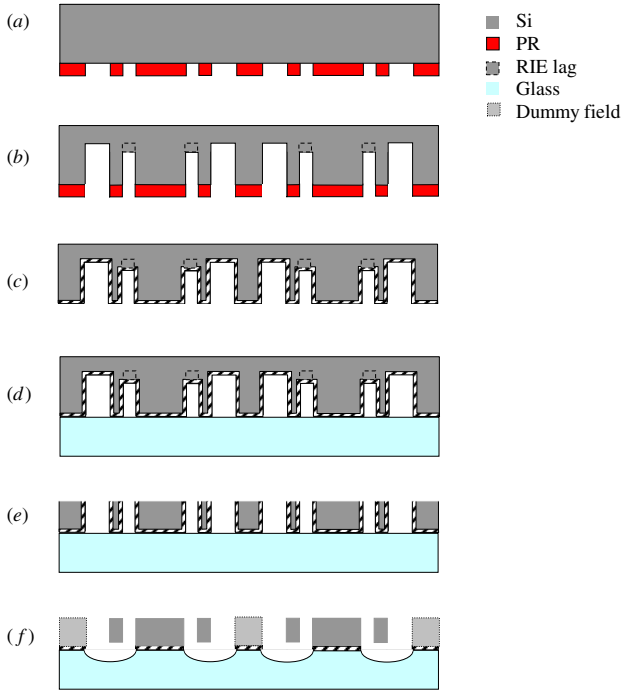

Figure 6. Fabrication by method II (method I with dummy fields): (*a*) silicon patterning using photo resist, (*b*) deep silicon etching, (*c*) protective layer deposition, (*d*) anodic bonding, (*e*) back-sided wet etching and (*f*) releasing of structure.

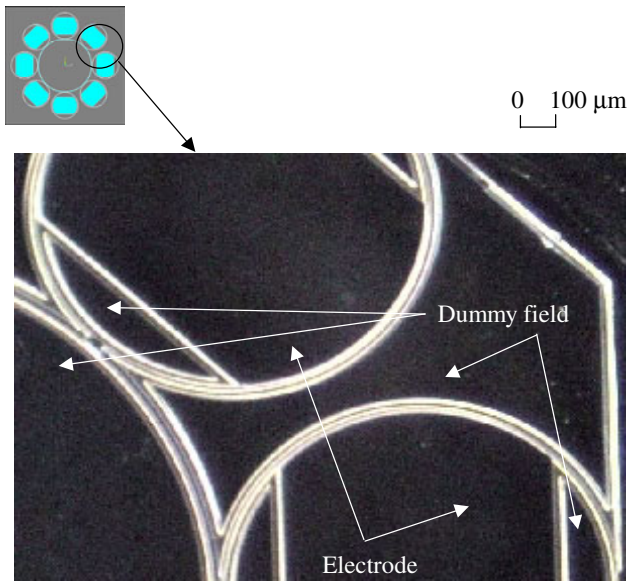

Figure 7. Photographs of the ring-type motion sensor fabricated using process shown in figure 6. Top view of the structure, 60 μm high.

is not necessary but still used for better yield. An inter-layer of 5000 Å nickel is deposited on the glass wafer. This layer prevents the bonding of dummy fields to the glass, as indicated in figure 8(*d*). It also prevents the bonding of the structure to the glass, ensuring that the structure is ideally released. An anodic bonder is used to bond the silicon wafer and the glass wafer. Back-sided wet etching removes the upper part of

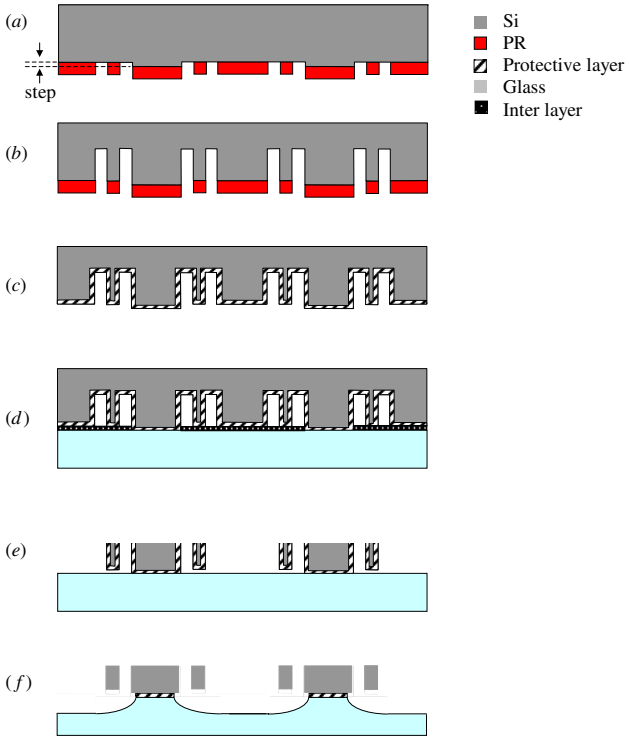

Figure 8. Fabrication by method III: (*a*) silicon patterning using photo resist, (*b*) deep silicon etching, (*c*) protective layer deposition, (*d*) anodic bonding, (*e*) back-sided wet etching and (*f*) releasing of structure.

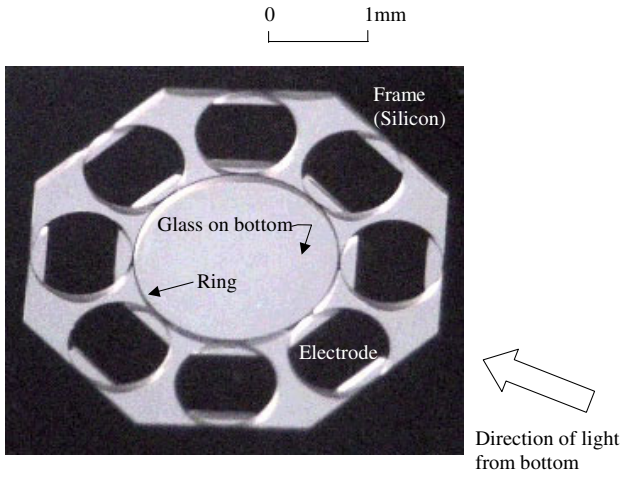

Figure 9. Photographs of the ring-type motion sensor fabricated using process in figure 8. Top view of a structure with a height of 180 μm, under back lighting through the glass.

the resulting SOI structure, yielding the structure depicted in figure 8(*e*). The structure is released by wet-etching the glass wafer, as depicted in figure 8(*f*). Figure 9 presents the resulting structure, whose height is 180 μm, which is satisfactory.

During the removal of the dummy fields, rather than increasing the step height which generates lithographic deficit, the inter-layer is introduced between the silicon and the glass in this method. Moreover, anodic bonding can generate a large

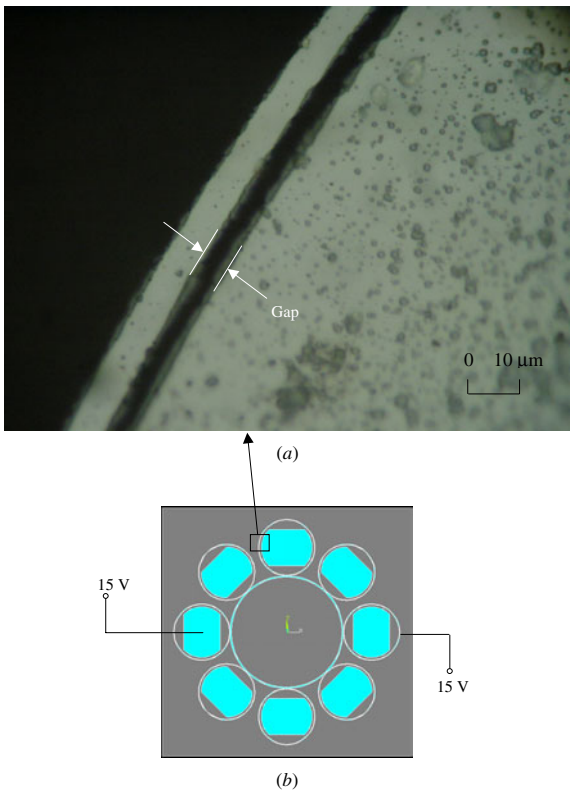

Figure 10. (*a*) Photograph of the ring-type motion sensor when the support ring is in a neutral position. (*b*) Electrical connections.

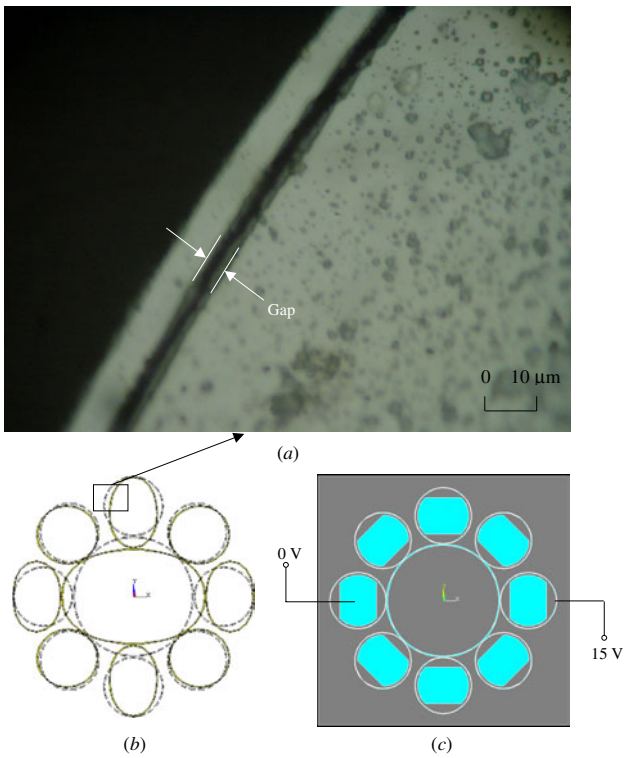

Figure 11. (*a*) Photograph of the ring-type motion sensor when the support ring is attracted by an electrode. (*b*) Deformed structure. (*c*) Electrical connections.

electrostatic force that collapses the suspended structure. In the absence of an inter-layer, the force would pull silicon and glass into contact with each other, causing undesired bonding.

Figure 10(*a*) shows that a gap exists between support ring and electrode. Figure 10(*b*) depicts the electrical connection where both the structural ground and driving electrode are connected to the same voltage. Figure 11(*a*) shows that the gap width is reduced when the support ring is attracted by electrode. Figure 11(*b*) shows that the support ring is deformed into an oval shape. Figure 11(*c*) depicts the electrical connection where the driving electrode is connected to a 0 V.

4. Sensitivity of sensor characteristics to manufacturing errors in fabrication

The ring radius, ring width, ring thickness, and gap between the ring and the electrode may all manifest manufacturing errors. Their sensitivities are estimated from the dimensional parameters, given in table 1. Single crystal silicon is a suitable material for its material properties, including density and Young's modulus, is stable. In fact, lithography rarely produces an error in the ring radius. Therefore, only by the error in the ring width that arises during fabrication affects the resonant frequency. The ring width designed here is 10 μm/ 20 μm, and the possible resultant error is from 1 to 2 μm, or 10%. The error in the width of the ring can cause an error in the width of the gap. The gap width used here is 2 μm, and so the error may strongly influence the performance of the sensor. The width of the gap increases as the width of the ring is reduced. An error in the gap width is the most common manufacturing error. Figure 12 plots the normalized sensitivities, listed in table 1, versus the change in the gap width. The width of the ring is designed to be ten times the width of the gap. The maximum error in the gap width is usually equal to the designed gap width because of the etching process used in this work. The normalized sensitivities of

Table 1. Dimensions of parameters.

	Symbol	Formula
Resonant frequency	ω_n	$\sqrt{\frac{E}{\rho}}\frac{w}{r^2}$
Electrostatic force	F_e	$\varepsilon V^{cc2}\frac{rt}{d^2}$
Coriolis force	F_c	$\Omega Q\varepsilon\sqrt{\frac{\rho}{E}}V^{cc2}\frac{tr^3}{wd^2}$
Rotation signal	V_{rot}	$\Omega Q\varepsilon\frac{\sqrt{\rho}}{E\sqrt{E}}V^{cc3}\frac{r^6}{w^4d^3}$
Acceleration signal	V_{acc}	$a\frac{\rho}{E}V^{cc}\frac{r^4}{dw^2}$
Signal-to-noise ratio for rotation	SNR(rot)	$\Omega Q\varepsilon^2\frac{1}{E}V^{cc3}\frac{r^3t}{w^5d^3}$
Signal-to-noise ratio for acceleration	SNR(acc)	$a\varepsilon\sqrt{\frac{\rho}{E}}V^{cc}\frac{r^3t}{d^2w}$

E: Young's modulus of material, ρ: material density, w: ring width, r: ring radius, ε: dielectric parameter, V^{cc}: static applied voltage, t: ring thickness, d: gap between ring and electrode, Ω: rotation rate, Q: quality factor, a: acceleration.

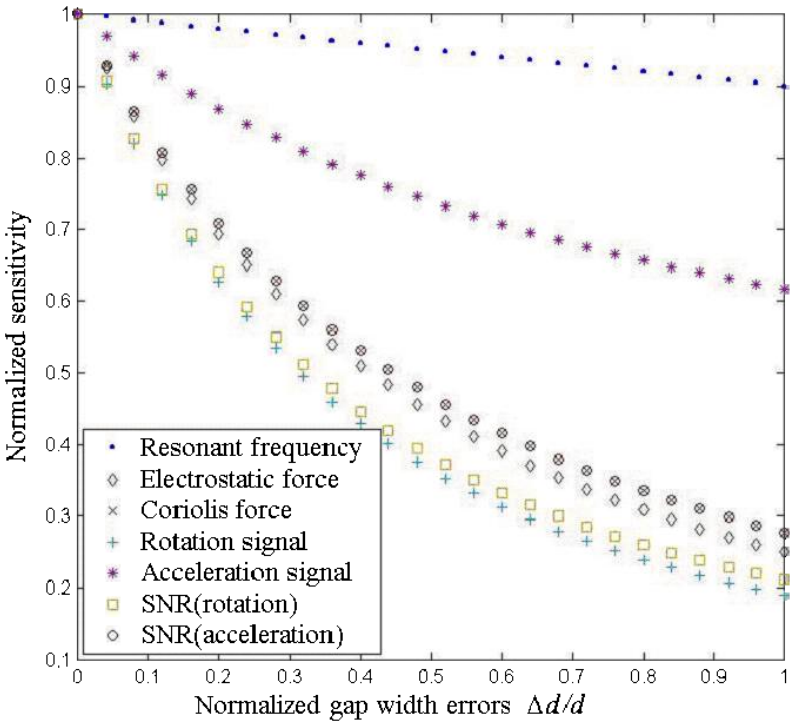

Figure 12. Normalized sensitivities of sensor characteristic of interest versus manufacturing errors in the gap width.

the sensor characteristics of interest to the inaccuracy in the gap width depicted in figure 12 show that every considered characteristic is degraded as the gap width increases. In the worst case, parameters such as the S/N ratio fall to around one-fifth of the designed values. The anisotropic characteristics of the structure can cause coupling of the vibration modes, which are related to crystallographic orientation of the silicon wafer [35], and the rotational misalignment in the fabrication. They can be eliminated by aligning the first mask with the crystal orientation of the wafer [36].

5. Conclusion

This work presents a micromachined motion sensor for sensing both yaw rate and linear acceleration. Three methods for fabricating the structure of the sensor are discussed. All of these methods include deep silicon etching, wafer bonding and back-sided etching. Any general design MEMS device suffers from aspect ratios that change with the structure, causing problems during etching, and particularly during dry etching. The effect of the aspect ratio is not of concern unless the etching depth is less than 20 μm. For applications in which the etching depth exceeds 20 μm, a protective layer is deposited to protect the structure from being inadvertently etched during back-sided etching. The actual height of the structure depends on the selectivity of the etching between the protective layer and substrate. The height of the structure remains limited. Adding dummy fields effectively suppresses ARDE. Adding dummy fields is a convenient and flexible means of designing and fabricating such a structure. Method III is a scheme for removing the dummy fields and increasing the height to 180 μm. This method reduces the probability of under-etching during the dry etching process, and increases the uniformity of the structure.

Acknowledgment

The authors thank the National Science Council of the Republic of China, Taiwan, for financially supporting this research under contract number NSC89-2212-E-009-062.

References

[1] Keister G W 1992 *Sensors and Transducers* ECN 21–32
[2] Baxter L K 1997 *Capacitive Sensors Design and Applications* (New York: IEEE Press)
[3] The vibration gyroscope 1993 *British Aerospace Systems and Equipment Report* TR5102
[4] Lawrence A 1993 *Modern Inertial Technology Navigation Guidance and Control* (New York: Springer) pp 163–81
[5] Lawrence A 1993 *Modern Inertial Technology Navigation Guidance and Control* (New York: Springer) pp 148–62
[6] Quick W H 1964 Theory of the vibrating string as an angular motion sensor *Trans. ASME, J. Appl. Mech.* **31** 523–34
[7] Gates W D 1968 Vibrating angular rate sensors may threaten the gyroscope *Electronics* **10** 130–4
[8] Lawrence A 1993 *Modern Inertial Technology Navigation Guidance and Control* (New York: Springer) pp 149–51
[9] Boocock D and Maunder L 1969 Vibration of a symmetry tuning fork *J. Mech. Eng. Sci.* **11** 4
[10] Parameswaran L, Hsu C and Schmidt M A 1995 A merged MEMS–CMOS process using silicon wafer bonding *Proc. IEEE Int. Electron Devices Mtg. (Washington, DC, Dec. 1995)*
[11] Greiff P, Boxenhorn B, King T and Niles L 1991 Silicon monolithic micromechanical gyroscope *Tech. Dig. 6th Int. Conf. Solid-State Sensors and Actuators, Transducers'91 (San Francisco, CA, June 1991)* pp 966–8

[12] Clark W A, Howe R T and Horowitz R 1996 Surface micromachined-axis vibratory rate gyroscope *Tech. Dig. Solid-State Sensor and Actuator Workshop (Hilton Head Island, SC, June 1996)* pp 283–7

[13] Juneau T and Pisano A P 1996 Micromachined dual input axis angular rate sensor *Tech. Dig. Solid-State Sensor and Actuator Workshop (Hilton Head Island, SC, June 1996)* pp 299–302

[14] Geiger W, Folkmer B, Merz J, Sandmaier H and Lang W 1998 A new silicon rate gyroscope *Proc. IEEE Micro Electro Mechanical Systems Workshop, MEMS'98 (Heidelberg, Germany, Feb. 1998)* pp 615–20

[15] Juneau T, Pisano A P and Smith J H 1997 Dual axis operation of a micromachined rate gyroscope *Tech. Dig. 9th Int. Conf. Solid-State Sensors and Actuators, Transducers'97 (Chicago, IL, June 1997)* pp 883–6

[16] Putty M W and Najafi K 1994 A micromachined vibrating ring gyroscope *Tech. Dig. Solid-State Sensor and Actuator Workshop (Hilton Head Island, SC, June 1994)* pp 213–20

[17] Gretillat F, Gretillat M-A and de Rooij N F 1999 Improved design of a silicon micromachined gyroscope with piezoresistive detection and electromagnetic excitation *IEEE J. Microelectromech. Syst.* **8** 243–50

[18] Sparks D R, Zarabadi S R, Johnson J D, Jiang Q, Chia M, Larsen O, Higdon W and Castillo-Borelley P 1997 A CMOS integrated surface micromachined angular rate sensor: it's automotive applications *Tech. Dig. 9th Int. Conf. Solid-State Sensors and Actuators, Transducers'97 (Chicago, IL, June 1997)* pp 851–4

[19] Ayazi F and Najafi K 2001 A HARPSS ploysilicon vibrating ring gyroscope *IEEE J. Microelectromech. Syst.* **10** 169–79

[20] Selvakumar A and Najafi K 1994 High density vertical comb array microactuators fabricated using a novel bulk/poly-silicon trench refill technology *Tech. Dig. Solid-State Sensor and Actuator Workshop (Hilton Head Island, SC)* pp 138–41

[21] Fox C H J and Hardie D S W 1984 *Vibratory Gyroscopic Sensors Symp. Gyro Technology* DGON

[22] Burdess J S and Wren T 1986 The theory of a piezoelectirc disc gyroscope *IEEE Trans. Aerosp. Electron. Syst.* **22** 411–8

[23] Gallacher B J, Burdess J S and Harris A J 2001 Principles of a three-axis vibrating gyroscope *IEEE Trans. Aerosp. Electron. Syst.* **37** 1333–43

[24] Loper E J and Lynch D D 1983 Projected system performance based on recent HRG test results *Proc. 5th Digital Avionics System Conf. (Seattle, WA, Nov. 1983)*

[25] Roylance L M and Angeel J B 1979 A batch-fabricated silicon accelerometer *IEEE Trans. Electron Devices* **26** 1911–7

[26] Seidel H, Riedel H, Jolbeck R, Muck G, Kuoke W and Koniger M 1990 Capacitive silicon accelerometer with highly symmetrical design *Proc. 5th Int. Conf. Solid State Sensors Actuators* pp 312–5

[27] Okada K 1995 Tri-axial piezo–electric accelerometer *Transducer'95, (25–29 June)* pp 566–9

[28] Puers B, Reynaret L, Soneyw W and Sansen W M C 1988 A new unaxial accelerometer in silicon based on the piezo-junction effect *IEEE Trans. Electronic Device* **35** 764–70

[29] Hiratsuka R, Duyn D C V, Otaredain T and de Vries P 1992 Design consideration for the thermal accelerometer *Sensors Actuators* A **32** 380–5

[30] Abbaspour-Sani E, Huang R S and Kwok C Y 1994 A linear electro-magnetic accelerometer *Sensors Actuators* A **44** 103–9

[31] Liu Cheng-Hsien and Kenny T W 2001 A high-precision, wide-bandwidth micromachined tunneling accelerometer *IEEE J. Microelectromech. Syst.* **10** 425–33

[32] Weng J H, Chieng W H and Lai J M Structural design and analysis of the micromachined ring-type vibrating microsensor sensing both yaw rate and linear acceleration *Sensors Actuators* submitted

[33] Yazdi N, Ayazi F and Najafi K 1998 Micromachined inertial sensors *Proc. IEEE* **86** 1640–59

[34] Bruschi H and Torzo G 1987 Method for accurate resonant frequency measurement with a phase modulated feedback loop *Rev. Sci. Inst.* **58** 2181–4

[35] Eley R, Fox C H J and McWilliam S 1999 Anisotropy effects on the vibration of circular rings made from crystalline silicon *J. Sound Vib.* **228** 11–35

[36] Lai J M, Chieng W H and Huang Y-C 1998 Precision alignment of mask etching with respect to crystal orientation *J. Micromech. Microeng.* **8** 327–9